Physics-informed transient stability assessment of microgrids

Priyanka Mishra and Peng Zhang ✉

ABSTRACT

With the integration of a voltage source converter (VSC), having variable internal voltages and source impedance, in a microgrid with high resistance to reactance ratio of short lines, angle-based transient stability techniques may find limitations. Under such a situation, the Lyapunov function can be a viable option for transient stability assessment (TSA) of such a VSC-interfaced microgrid. However, the determination of the Lyapunov function with the classical method is very challenging for a microgrid with converter controller dynamics. To overcome such challenges, this paper develops a physics-informed, Lyapunov function-based TSA framework for VSC-interfaced microgrids. The method uses the physics involved and the initial and boundary conditions of the system in learning the Lyapunov functions. This method is tested and validated under faults, droop-coefficient changes, generator outages, and load shedding on a small grid-connected microgrid and the CIGRE microgrid.

Modern microgrids often coordinate a group of generating units interfaced with voltage source converters (VSCs) and a set of loads with the capability to provide smooth transformation between the grid-connected and islanded modes. Such features and flexibility improve the customers' electricity resilience under grid failures[1]. However, the resilience benefit offered by a microgrid will be in jeopardy if it cannot tolerate disturbances and loses its stability[2]. Therefore, proper transient stability assessment (TSA) is required for both offline design and online operation of microgrids[3].

The ability of the synchronous generators to uphold their synchronism state despite severe disturbances in the system makes the rotor angle an inherent means for TSA of the system[4, 5]. However, full-scale VSCs being integrated into the microgrid have no rotating parts; therefore, rotor angle stability finds limitations for VSC-interfaced microgrids. Synchronverters[6] also known as virtual synchronous generators[7] or virtual synchronous machines[8] are developed to improve the angle instability mechanism of the VSC. Despite these propositions, microgrids fail to satisfy the rotor angle stability criteria.

Various control strategies, such as master/slave, current sharing, and frequency/angle droop methods[3, 9] is implemented in VSCs to support the power system, satisfying fault-ride through (FRT) requirements of the grid codes[10]. Both the master/slave and current sharing control require communication[3], which can not decide in case of communication link failure. Whereas, droop methods do not require communication among the VSCs and are suitable for distributed implementation. However, these droop control options change the internal voltage and source impedance of VSC unlike the constant source impedance of synchronous generator during fault[11]. Moreover, microgrid lines are short in length and possess a low reactance to resistance ratio[12]. These features make the VSC-interfaced microgrid a nonlinear system and violate the assumptions made in developing the power-angle curve, which limits the applicability of equal-area criteria for TSA of microgrids[13]. Thus, the dynamics of VSCs and microgrids need to be analyzed under large disturbances to assess the transient stability of such nonlinear systems.

Several direct energy methods are proposed for the stability assessment of microgrids. These energy functions are specific forms of Lyapunov functions that guarantee the system's convergence to stable equilibrium points. The method in Ref. [14] leverages the energy function approach, assuming lossless lines, to certify the stability of an equilibrium point. However, the method is not valid for lossy microgrid lines. Without the lossless-line assumption, the method[3] decouples the slow dynamics via linearization[5] and fast dynamics by linear matrix inequality[15] in a microgrid. However, the proposed framework only provides a binary answer to the TSA of the microgrids. It is equally important to estimate the extent of disturbances that can be tolerated by microgrids. Methods in Refs. [16] and [17] construct a quadratic Lyapunov function that can be used for TSA of a power system with line loss. However, TSA based on quadratic Lyapunov functions may be overly conservative. The method in Ref. [18] leverages the sum of square technique to construct a Lyapunov function for TSA of networked microgrids. However, the technique is computationally intractable when addressing large systems.

Various methods leveraging the advances in neural networks (NNs) and control theory are proposed to provide a rigorous and scalable TSA in VSC-interfaced microgrids[19–21]. However, these methods suffer from a lack of trust on the side of grid operators due to the NNs' black-box nature. Moreover, machine learning approaches are based on data. Acquirement of high-quality real-time data sets for both normal and abnormal situations equally well is a challenging task, as abnormal events tend to be rare. The generation of such data sets through simulations will further increase the computational burden that cannot be disregarded. To overcome the problem of limited availability of datasets, physical knowledge of the model is directly incorporated into the neural networks. In Refs. [22] and [23], a physics-informed neural network (PINN) is proposed, which introduces the governing equations of nonlinear systems in the training process of a neural network and allows the screening of more than a hundred contingencies at the same time that conventional methods would only screen a single one. Incorporating the differential-algebraic equations inside the

Department of Electrical and Computer Engineering, Stony Brook University, NY 11794, USA
Address correspondence to Peng Zhang, P.Zhang@stonybrook.edu

neural network training, PINNs can learn through the incorporated first principles models instead of using external massive training datasets.

This paper presents a physics-informed Lyapunov-based transient stability assessment of VSC-interfaced microgrids. The method learns a neural network structured Lyapunov function in state space, considering the required dynamics of the Lyapunov function. In addition, the problem of TSA due to the angle instability mechanism of VSC, short microgrid lines with high resistance to reactance ratio, and dynamics of the microgrid are presented through mathematical deduction, expounding the difference between VSC and synchronous generators. The performance of the proposed method is tested for a three-bus grid-connected microgrid and a CIGRE microgrid. The comparative assessment shows the advantage of the proposed PINN approach in prediction accuracy and evaluation loss over the standard neural network method for TSA of the VSC-interfaced microgrid.

The contributions of this paper are fourfold: (i) a mathematical expression for transient stability analysis of VSC is derived; (ii) the computational complexities of conventional Lyapunov function in TSA are studied, considering the VSC control strategies and microgrid dynamics; (iii) a PINN-enabled Lyapunov function is learned in state-space, and (iv) extensive validations of the efficacy of the data-free, physics-informed approach to TSA. The remainder of this paper is organized as follows: Section 1 analyses the challenges associated with angle stability analysis for VSC-interfaced microgrids. Section 2 describes the dynamics of the VSC-interfaced microgrid and associated challenges with the mathematical formulation of the Lyapunov function. Section 3 describes a PINN-based Lyapunov approach to TSA. Section 4 validates the new tool on two microgrids, followed by the comparative assessment in Section 5. Section 6 concludes the paper.

1 Challenge with angle stability analysis for VSC-interfaced microgrid

Satisfying FRT requirements of the grid codes, VSC remains connected to the grid even during fault conditions[24]. The fast dynamics of the converter, operating at a high pulse width modulation (PWM) frequency, allows it to survive even transient disturbances. Therefore, the VSC output voltage and current behavior are controlled by the associated control strategies during transient conditions. Intermittency and variability further complicate the controller operation, resulting in varying internal voltage and source impedance of VSC, which further affect the relation of output power and angle difference of VSC and grid bus voltages. This influences the angle stability analysis for TSA of the microgrid in the presence of VSC. Thus, the impact of control algorithms on VSC output power and bus voltage angle is studied in the context of transient (angle) stability. An analysis is carried out in the following.

Figure 1 shows an impedance diagram of VSC connected to the grid. $E_{\mathrm{VSC}}\angle\varphi$ and $E_{\mathrm{g}}\angle 0$ are internal and bus voltages of VSC and grid, respectively. $Z_{\mathrm{VSC}}\angle\theta_{\mathrm{VSC}} = R_{\mathrm{VSC}} + jX_{\mathrm{VSC}}$ and $Z_{\mathrm{line}}\angle\theta_{\mathrm{line}} = R_{\mathrm{line}} + jX_{\mathrm{line}}$ are impedances of VSC source and line, respectively. R and X refer to resistance and reactance, respectively. $V_{\mathrm{o}}\angle\delta$ and $I_{\mathrm{o}}\angle\phi$ are output voltage and current, respectively. Here, subscripts VSC, g, and line refer to the VSC source, grid, and line, respectively.

The output complex power S of VSC can be expressed as in Ref. [25].

$$S = V_{\mathrm{o}}\angle\delta\,(I_{\mathrm{o}}\angle\phi)^{*}, \tag{1}$$
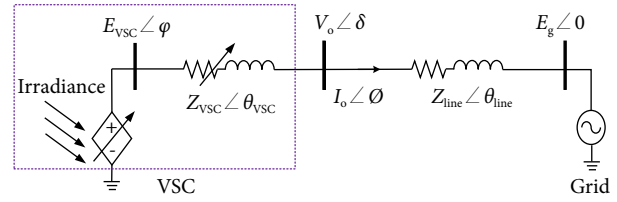

Fig. 1 Impedance diagram of grid-connected VSC with variable internal source voltage E_{VSC} and associated impedance Z_{VSC}.

where

$$V_{\mathrm{o}}\angle\delta = E_{\mathrm{VSC}}\angle\varphi - Z_{\mathrm{VSC}}\angle\theta_{\mathrm{VSC}}\,I_{\mathrm{o}}\angle\phi, \tag{2}$$

and

$$I_{\mathrm{o}}\angle\phi = \frac{V_{\mathrm{o}}\angle\delta - E_{\mathrm{g}}\angle 0}{Z_{\mathrm{line}}\angle\theta_{\mathrm{line}}}. \tag{3}$$

Substituting Eqs. (2) and (3) in Eq. (1) and separating real and imaginary parts of S, we have the active power P as given by,

$$P = \frac{E_{\mathrm{VSC}}V_{\mathrm{o}}Z_{\mathrm{line}}\sin(\varphi+\theta_{\mathrm{line}})}{R_{\mathrm{line}}^2 + X_{\mathrm{line}}^2}\sin\delta$$
$$+\frac{E_{\mathrm{VSC}}V_{\mathrm{o}}Z_{\mathrm{line}}\cos(\varphi+\theta_{\mathrm{line}}) + 2R_{\mathrm{VSC}}V_{\mathrm{o}}E_{\mathrm{g}}}{R_{\mathrm{line}}^2 + X_{\mathrm{line}}^2}\cos\delta \tag{4}$$
$$+\frac{E_{\mathrm{VSC}}E_{\mathrm{g}}Z_{\mathrm{line}}\cos(\varphi+\theta_{\mathrm{line}}) - R_{\mathrm{VSC}}(V_{\mathrm{o}}^2+E_{\mathrm{g}}^2)}{R_{\mathrm{line}}^2 + X_{\mathrm{line}}^2}.$$

The partial derivative of active power P in Eq. (4) with respect to δ is given by,

$$\frac{\partial P}{\partial\delta} = P_{\max}\,\sin(\mu-\delta), \tag{5}$$

where

$$P_{\max} = \left(\left(\frac{E_{\mathrm{VSC}}V_{\mathrm{o}}Z_{\mathrm{line}}\sin(\varphi+\theta_{\mathrm{line}})}{R_{\mathrm{line}}^2 + X_{\mathrm{line}}^2}\right)^2\right.$$
$$\left.+\left(\frac{E_{\mathrm{VSC}}V_{\mathrm{o}}Z_{\mathrm{line}}\cos(\varphi+\theta_{\mathrm{line}}) + 2R_{\mathrm{VSC}}V_{\mathrm{o}}E_{\mathrm{g}}}{R_{\mathrm{line}}^2 + X_{\mathrm{line}}^2}\right)^2\right)^{1/2}, \tag{6}$$

$$\mu = \arctan\left(\frac{E_{\mathrm{VSC}}Z_{\mathrm{line}}\sin(\varphi+\theta_{\mathrm{line}})}{E_{\mathrm{VSC}}Z_{\mathrm{line}}\cos(\varphi+\theta_{\mathrm{line}}) + 2R_{\mathrm{VSC}}E_{\mathrm{g}}}\right). \tag{7}$$

From Eq. (5), the unique criteria of stability is satisfied if,

$$\frac{\partial P}{\partial\delta} > 0,\ \forall\ 0 < \delta < \mu. \tag{8}$$

The active power attains its maximum value when the maximum value of δ is equal to μ in Eq. (7).

$$\delta_{\max} = \arctan\left(\frac{E_{\mathrm{VSC}}Z_{\mathrm{line}}\sin(\varphi+\theta_{\mathrm{line}})}{E_{\mathrm{VSC}}Z_{\mathrm{line}}\cos(\varphi+\theta_{\mathrm{line}}) + 2R_{\mathrm{VSC}}E_{\mathrm{g}}}\right). \tag{9}$$

Here, $\delta_{\max}$ is a function of $E_{\mathrm{VSC}}\angle\varphi$, $Z_{\mathrm{VSC}}\angle\theta_{\mathrm{VSC}}$ and $Z_{\mathrm{line}}\angle\theta_{\mathrm{line}}$. Among them, $E_{\mathrm{VSC}}\angle\varphi$ and $Z_{\mathrm{VSC}}\angle\theta_{\mathrm{VSC}}$ depend on converter current constraints and control strategies. With the change in associated controller modes, these values of internal voltage and source impedance vary. Furthermore, $Z_{\mathrm{line}}\angle\theta_{\mathrm{line}}$ depends on the line parameters of a microgrid, which is resistive in nature, unlike the inductive nature of transmission lines. Therefore, the existing P–δ curve to study the stability of the conventional system may be different for VSC.

To study the impact of control strategies on the $P_{\max}$ and $\delta_{\max}$, we consider a 25 kV, 60 Hz system with 100 kW VSC connected at one end, as shown in Figure 1. The nominal voltage droop is

chosen as 2% at the maximum reactive power output of VSC. $Z_{line} = 3.64\angle 53°\ \Omega$. The method for the computation of the internal voltage and source impedance is presented in Appendix. In the following, the impact of control options on the different parameters used in Eqs. (6) and (9) to describe $P–\delta$ curve are discussed in detail.

1.1 Variable VSC source impedance

VSC's output current pattern varies with the change in irradiation level, maintaining the balanced output voltage. This results in the variation in the internal voltage and source impedance of the converter. Figure 2 shows the variation of internal voltage E_{VSC} and source impedances R_{VSC} and X_{VSC} of VSC with irradiance level. The decrement in irradiation increases the internal voltage and source impedance of VSC or vice versa. When R_{VSC} reduces from 0.31 pu to 0.03 pu with the increment in irradiance from $100\ W/m^2$ to $1000\ W/m^2$, P_{max} in Eq. (6) reduces from 2.7 pu to 1.8 pu. Similarly, δ_{max} in Eq. (9) reduces in inversely proportional manner from $77.8°$ to $40.9°$, as shown in Figure 3. This confirms that δ_{max} will be less than $90°$ for the VSC-interfaced microgrid, whereas it is equal to $90°$ for the ideal characteristic.
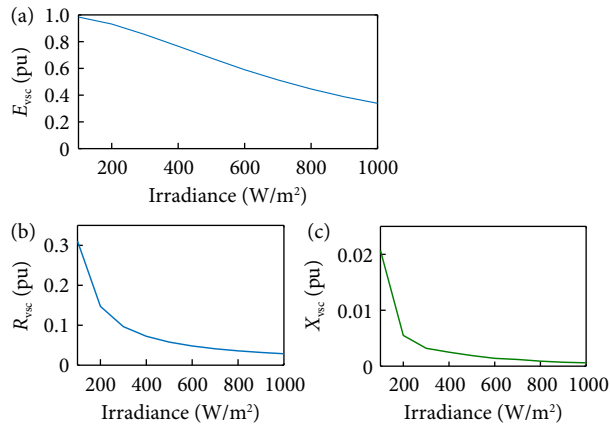

Fig. 2 Variation of (a) internal voltage E_{VSC}, and associated source impedance of VSC: (b) equivalent resistance R_{VSC}, and (c) equivalent reactance X_{VSC} with irradiance levels.
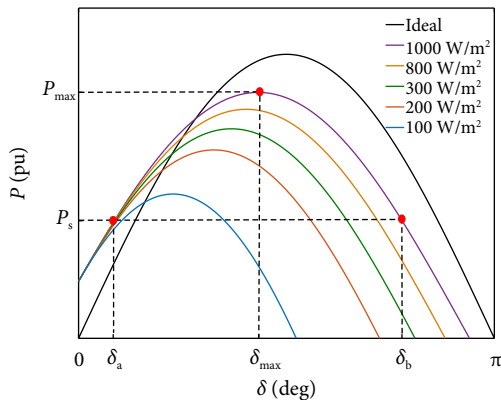

Fig. 3 $P–\delta$ characteristic curves for different irradiance levels of VSC and an ideal characteristic curve.

1.2 High R/X ratio of microgrid line

Because of the resistive nature of the microgrid lines (i.e. $R_{line}/X_{line} = 2.3 > 1$), the line impedance angle θ_{line} lies in the range of $0 - \pi$, whereas it is approximately $90°$ for the highly inductive

transmission line. Thus, δ_{max} and P_{max} are the decreasing function of $Z_{line}\angle\theta_{line}$.

1.3 $P–\delta$ curve for VSC-interfaced microgrid

For the ideal case, VSC system pursues the following conditions:

   (i) VSC internal voltage angle is set for $\varphi = 0°$.
   (ii) The line parameters are mainly inductive, i.e. $\theta_{line} = 90°$.
   (iii) The source impedance of VSC is set for $R_{VSC} \approx 0$.

The corresponding δ_{max} will be approximately $90°$, as shown as black color curve. However, due to the significant impact of control strategies on VSC, $\varphi \neq 0°$ and $R_{VSC} \neq 0$. Similarly, a high R/X ratio of the line causes $\theta_{line} \neq 90°$. Therefore, $\delta_{max} \neq 90°$ and P_{max} have different values for each $P–\delta$ curves at $100, 200, 300, 800$ and $1000\ W/m^2$ solar irradiance, as shown in Figure 3. Note that curves have an offset at $\delta = 0°$ due to the constant part in Eq. (6).

Moreover, the inertia causes inevitable swings on the rotor of a generator in a disturbance. VSC has no rotating part and output power and angle relation depend on the control scheme. As shown in Figures 4(a) and 4(b), with the increases in irradiance, P becomes large, whereas δ does not change significantly and follows a monotonically increasing trend. Therefore, if δ is equal to δ_a at the point on $P–\delta$ curve, the system satisfies the stability criteria (i.e., $\partial P/\partial\delta > 0$). For point b at power P_s, the stability criteria change (i.e., $\partial P/\partial\delta < 0$), and the behavior of VSC change inversely such that the system loses stability. Therefore, the transient stability assessment of the VSC-interfaced microgrid is not possible with the conventional approaches. A method is needed to access the transient stability of microgrids with a high R/X ratio of lines connecting VSC with variable internal voltage and source impedance.
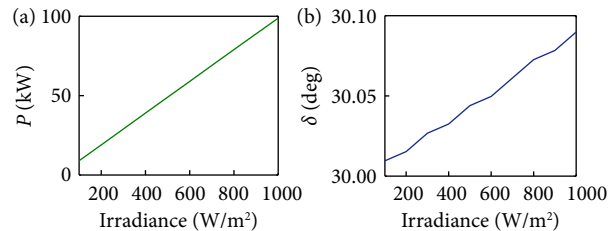

Fig. 4 Variation of output (a) active power P, and (b) angle δ of VSC with irradiance pattern.

2 Challenges with mathematical formulation of lyapunov function for VSC-interfaced microgrid

As discussed in Section 1, the associated control options have significant impacts on the system behavior. A time domain analysis has been carried out in this section to explain the dynamics of the microgrid. After linearization, the system dynamics can be defined as in Ref. [12].

$$\begin{bmatrix} \Delta\dot{x}_{VSC} \\ \Delta\dot{i}_{line}^{dq} \\ \Delta\dot{i}_{load}^{dq} \end{bmatrix} = \begin{bmatrix} A_{VSC} & . & . \\ . & A_{line} & . \\ . & . & A_{load} \end{bmatrix} \begin{bmatrix} \Delta x_{VSC} \\ \Delta i_{line}^{dq} \\ \Delta i_{load}^{dq} \end{bmatrix}, \quad (10)$$

where A_{VSC} is a VSC controller matrix, which includes droop coefficients of reactive power-voltage and power-frequency droop controls, steady-state frequency of the system, the cut-off frequency of the low-pass filter, and inductance and capacitance of the inverter filter. A_{line} includes the parameters of the line. A_{load} includes the load parameters. i_{line}^{dq} and i_{load}^{dq} are dq components of the currents flowing in the line and load, respectively. Δx_{VSC} represents the states of s converters.

$$[\Delta x_{\text{VSC}}] = [\Delta x_{\text{VSC\_1}}...\Delta x_{\text{VSC\_i}}...\Delta x_{\text{VSC\_s}}]^{\text{T}}, \tag{11}$$

where the states of each converter i are

$$\Delta x_{\text{VSC\_i}} = [\Delta\delta_i\ \Delta P_i\ \Delta Q_i\ \Delta\phi_{dqi}\ \Delta\gamma_{dqi}\ \Delta i_{ldqi}\ \Delta v_{odqi}\ \Delta i_{odqi}]^{\text{T}}. \tag{12}$$

Considering a microgrid of m nodes with s converters, p lines, and q load points, the system has a dimension of $13 \times s + 2 \times p + 2 \times q$. Here, the reference frame of converter number 1 is taken as the common reference frame. The differential equations can be expressed in the matrix form as follows:

$$\dot{x} = A_{mg}x, \tag{13}$$

where

$$x = [\Delta x_{\text{VSC}}\ \Delta i_{\text{line}_{DQ}}\ \Delta i_{\text{load}_{DQ}}]^{\text{T}},$$

$$A_{mg} = \begin{bmatrix} A_{\text{VSC}} & . & . \\ . & A_{\text{line}} & . \\ . & . & A_{\text{load}} \end{bmatrix}.$$

Assuming, the microgrid in Eq. (13) is in equilibrium at $x = 0$.

The stability notions of interest for the dynamic systems can be certified if a Lyapunov function can be found. A smooth function $V : x \rightarrow R_{\geq 0}^m$ is a Lyapunov function of the system (13) with equilibrium point 0 if the following conditions hold:

$$\begin{aligned} V(0) &= 0, \\ V(x) &> 0 \ \forall\, x \in S, \ \backslash 0, \\ \dot{V}(x) &\leq 0 \ \forall\, x \in S, \ \backslash 0. \end{aligned} \tag{14}$$

where S is the stability region. For each equilibrium point $x = 0$, there exists a unique Lyapunov function. However, for such a complex system with variable system parameters, the determination of the Lyapunov function is very challenging. Therefore, a machine learning approach is proposed in this work to find a Lyapunov function for such a microgrid to assess its transient stability.

3 Physics-informed method

A Physics-informed Lyapunov function is proposed to assess the transient stability of the microgrid in the presence of a high share of VSCs. The method considers the initial and boundary conditions and governing equations to construct a Lyapunov function. The function is learned by minimizing the loss function. The details of the proposed approach are discussed in the following subsections.

3.1 Lyapunov function with physics informed neural network structure

PINN Lyapunov function is approximated by a deep neural network about how well it matches the governing partial differential equations and initial and boundary conditions, as shown in Figure 5. The deep neural network has several hidden layers and one output layer. The inputs to the first hidden layer are the states x in Eq. (13) which are time-dependent. The input $x \in R^m$ and output of the first hidden layer $v_1 \in R^n$ are related via relation in as defined by,

$$v_1(x) = \tanh(b_1 + w_1 x), \tag{15}$$

where $b_1 \in R^n$ and $w_1 \in R^{n \times m}$ are bias and weight matrices, respectively, of the first layer. n is the number of neurons in each layer. Hyperbolic tangent function tanh(.) is chosen as an activation function in this study. Similarly, v_1 is an input for the second hidden layer, and output $v_2 \in n$ of the layer can be defined as

$$v_2(x) = \tanh(b_2 + w_2 v_1), \tag{16}$$

where $b_2 \in R^n$ and $w_2 \in R^{n \times n}$ are bias and weight matrices, respectively, of the second layer. This process continues in the same manner up to the last output layer. The output of the output layer is $V \in R$, which is interpreted as the Lyapunov function evaluated at vector x. V is related to x via a relation given in Ref. [26], which is defined by,

$$V(x) = \tanh(b_l + w_l\tanh(b_{l-1} + w_{l-1}\tanh(... + w_1 x))). \tag{17}$$

where l is the total number of layers in the deep neural network. $b_l \in R$ and $w_l \in R^{1 \times n}$ are bias and weight matrices, respectively, of the output layer. Eq. (17) indicates that the Lyapunov function V depends on the input states and the weight and bias matrices.

The first-order derivative of the Lyapunov function with respect to time can be computed as in Eq. (18).

$$\dot{V}(x) = \frac{\mathrm{d}V}{\mathrm{d}t} = \frac{\partial V}{\partial x}\frac{\partial x}{\partial t}, \tag{18}$$

For V in Eq. (17), $\partial V/\partial x$ will be,

$$\frac{\partial V}{\partial x} = (1 - V^2)w_l\frac{\partial(\tanh(b_{l-1} + w_{l-1}\tanh(... + w_1 x)))}{\partial x}, \tag{19}$$

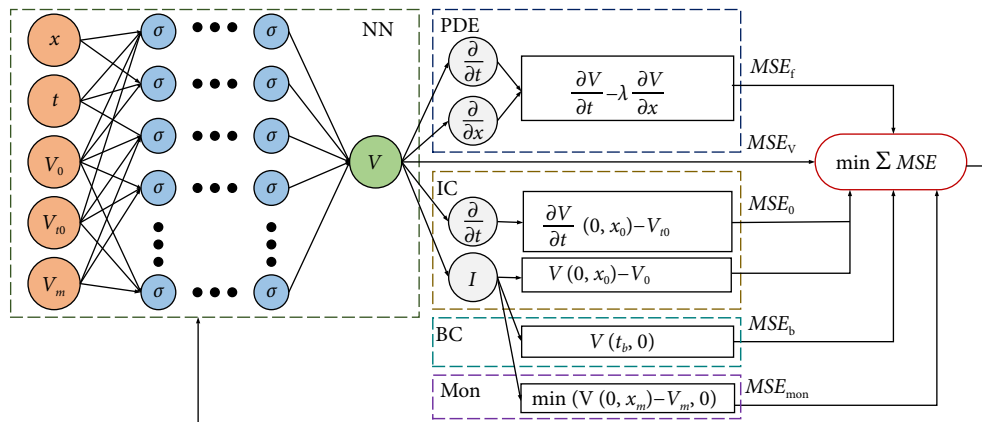**Fig. 5** Schematic of PINN for Lyapunov function governing equation. NN: deep neural network, PDE: partial derivative equation with parameter λ, IC: initial conditions, BC: boundary conditions, and Mon: monotonically decreasing conditions.

Substituting $\partial V/\partial x$ from Eq. (19) in Eq. (18) and $\partial x/\partial t = \dot{x} = A_{mg}x$ from Eq. (13) in Eq. (18), the differential equation $\dot{V}$ can be expressed in a simplified matrix form as follows,

$$\dot{V}(x) = (1 - V^2)\, w_l\, A_{mg}\, x\, \gamma, \qquad (20)$$

where

$$\gamma = \frac{\partial}{\partial x}(\tanh(b_{l-1} + w_{l-1}\tanh(... + w_1 x))).$$

which includes the states, weight and bias matrices of various neutrons at different layers. The above equation reveals that the derivative $\dot{V}$ requires the dynamics of the microgrid in Eq. (13), which may not be available for this purpose.

To solve the problem of data-driven solution of non-linear partial differential equation in Eq. (18) to find V with inequality constraints in Eq. (14), let us define $f(t, x)$ to be given by,

$$f := V_t + N[V; \lambda], \quad x \subset R^m, \quad t \in [0, T], \qquad (21)$$

with initial conditions,

$$V(0, x) = C \quad and \quad V_t(0, x) = -C, \qquad (22)$$

and boundary conditions,

$$V(t, 0) = 0. \qquad (23)$$

where $V(t, x)$ denotes the latent (hidden) solution and is approximated by a deep neural network. $N[V; \lambda]$ is a nonlinear operator parameterized by system parameter λ. This assumption along with Eq. (21) results in a physics-informed neural network $f(t, x)$. This network can be derived by applying the chain rule for differentiating compositions of functions using automatic differentiation. Here, the subscript t denotes partial differentiation in time. C is a constant. Its value is set to 0 at $V(0, 0)$ in training.

3.2 Loss minimization

The shared parameters of the neural networks $V(t, x)$ and $f(t, x)$ along with the parameter λ of the differential operator, considering initial and boundary conditions, can be learned by minimizing the mean squared error loss.

$$MSE = MSE_V + MSE_f + MSE_0 + MSE_b + MSE_{Mon}, \qquad (24)$$

where

$$MSE_V = \frac{1}{N_V}\sum_{i=1}^{N_V}|V(t_V^i, x_V^i) - V^i|^2, \qquad (25)$$

$$MSE_f = \frac{1}{N_f}\sum_{i=1}^{N_f}|f(t_f^i, x_f^i)|^2, \qquad (26)$$

$$MSE_0 = \frac{1}{N_0}\sum_{i=1}^{N_0}(|V(0, x_0^i) - V_0^i|^2 + |V_t(0, x_0^i) - V_{t0}^i|^2), \qquad (27)$$

$$MSE_b = \frac{1}{N_b}\sum_{i=1}^{N_b}|V(t_b^i, 0)|^2, \qquad (28)$$

$$MSE_{Mon} = \frac{1}{N_m}\sum_{i=1}^{N_m}|\min(V(0, x_m^i) - V_m^i, 0)|^2. \qquad (29)$$

Here, the interpretation of the Loss function in Eq. (24) is presented as follows. The first term MSE_V corresponds to the training data $(t_V^i, x_V^i, V^i)_{i=1}^{N_V}$ on $V(t, x)$. Second term MSE_f corresponds to a finite set of collocation points (t_f^i, x_f^i). Third term MSE_0 corresponds to the loss on the initial data $(x_0^i, V_0^i)_{i=1}^{N_0}$. Fourth term MSE_b enforces the periodic boundary conditions. $(t_b^i, x_b^i)_{i=1}^{N_b}$ corresponds to the collocation points on the boundary. Fifth term MSE_{Mon} corresponds to the monotonicity loss to ensure that V must be monotonically decreasing in the range S so that $\dot{V} \leq 0$. $(x_m^i)_{i=1}^{N_m}$ corresponds to the collocation points. L-BFGS optimizer is used to minimize the mean square error loss of Eq. (24) in this study. The derivatives of the network output V with respect to the input x are evaluated exactly and efficiently via back-propagation. It includes information on VSC control dynamics such as droop controls, lines, and loads, as in Eq. (13). The details of VSC control dynamics are given in Ref. [12].

4 Results

The proposed approach has been evaluated on two systems: first for three bus grid-connected microgrids to analyze the impact of the fault and change of droop control; second for the CIGRE microgrid to analyze the impact of generator outage and load shedding on the transient stability of the system. All experiments in this section are conducted on a DELL (2.5 GHz Intel Core i7 11th Gen) with Python 3.9.12 and TensorFlow 2.9.1.

4.1 Grid-connected microgrid

Consider a 220 V (per phase RMS), 50 Hz microgrid of three buses with three VSCs of 10 kVA each, two lines, and two resistive loads of 7.3 kW and 5.8 kW, respectively[12]. The detailed system diagram with VSCs ratings, loads, and line parameters is shown in Figure 6. Frequency droop of 0.3% at the maximum real power output and voltage droop of 2% at the maximum reactive power output is chosen for all VSCs to equally share the power. After training the proposed algorithm 500 times which takes 42.1882 s, the learned output is a Lyapunov function. Figures 7(a) and 7(b) show the learned Lyapunov function and its time derivative, respectively. The learned function is positive definite and its time derivative is negative definite, which suggests that the function learned is a Lyapunov function and can be used for TSA of the grid-connected microgrid.
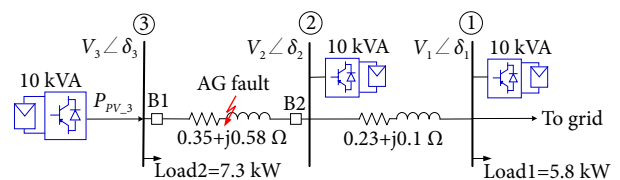

Fig. 6 Impedance diagram of grid-connected VSC with AG fault in the middle of line 23.

For the system, two cases are studied. Case-A discusses the performance of the method after the clearance of phase A-to-ground (AG) fault with 0 Ω fault resistance from line 23. Case-B presents the impact of change in reactive power-voltage droop coefficient on the system's transient stability.

Case-A   Impact of fault clearance

A bolted AG fault is created in the middle of the line connecting bus 2 and bus 3, resulting in 0 value of the output power of VSC at bus 3. The fault is removed at 0 s. The time-domain simulation result of the power output and voltage angle of the VSC at bus 3 are shown in Figures 8(a) and 8(b) with initial conditions $x(0)$ of $0°$ and 0 kW. It is observed that all the interface variables δ_3 and
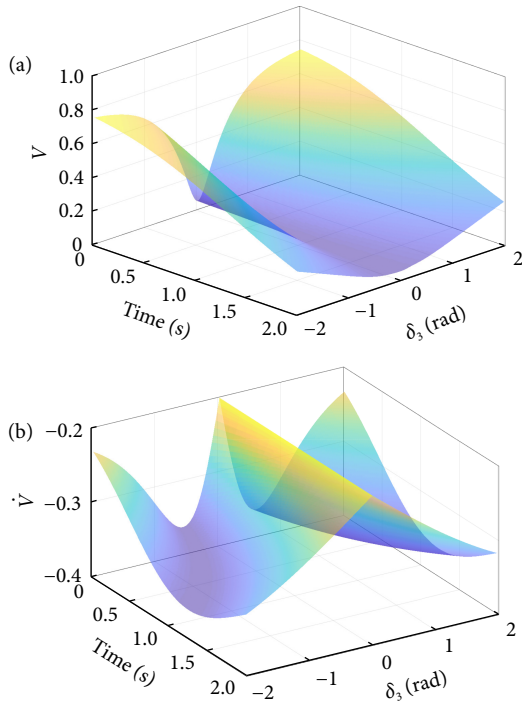
Fig. 7 (a) Lyapunov function and (b) time derivative of Lyapunov function for a grid-connected microgrid under stable condition.
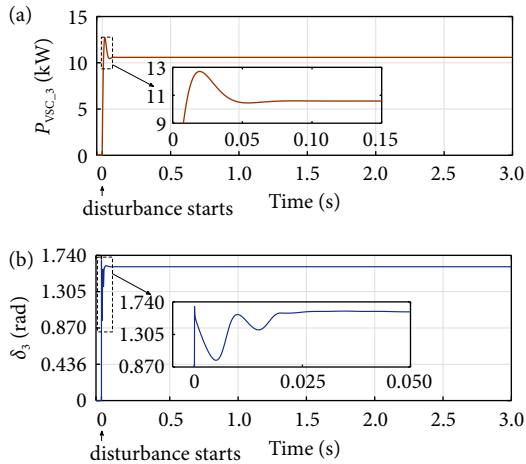

Fig. 8 (a) Power output of VSC and, (b) voltage angle at bus 3 after the removal of fault in grid-connected system.

$P_{\text{VSC\_3}}$ tend to return to their equilibrium point after the removal of the fault at 0 s. This ensures the stability of the system after a disturbance. Similarly, with the initial condition, the learned Lyapunov function in Figure 7(a) is $V(x(0)) = 0.05 > 0$ and it strictly decreases with time before the system reaches the equilibrium point. This validates the applicability of the proposed approach as the results of the proposed method match the simulation results.

Case-B Impact of droop coefficient variation

In the real system, there might be a case when the parameters of the controller are not properly tuned, which may affect the stability of the system. In such a situation also, the physics-informed Lyapunov function finds application in determining the stability of the VSC-interfaced microgrid. To demonstrate the situation, a hypothetical case is simulated where the droop coefficient of the active power-frequency droop control of VSC 3 at bus 3 is changed to −4%, while other system parameters are kept same in

the given system, shown in Figure 6. After training the proposed algorithm for the modified system, the learned Lyapunov function and its time derivative are shown in Figures 9(a) and 9(b), respectively. The learned function is negative and its time derivative is positive for various combinations of δ_3 and $P_{\text{VSC\_3}}$, such as $\delta_3 = 0$ rad and $P_{\text{VSC\_3}} = 0$ pu. Results confirm that the given microgrid with −4% droop coefficient for VSC 3 is not satisfying the Lyapunov stability criteria mentioned in Eq. (14), and is unstable. Therefore, the proposed physics-informed Lyapunov function is an essential tool for determining the stability of microgrids having variable control dynamics.
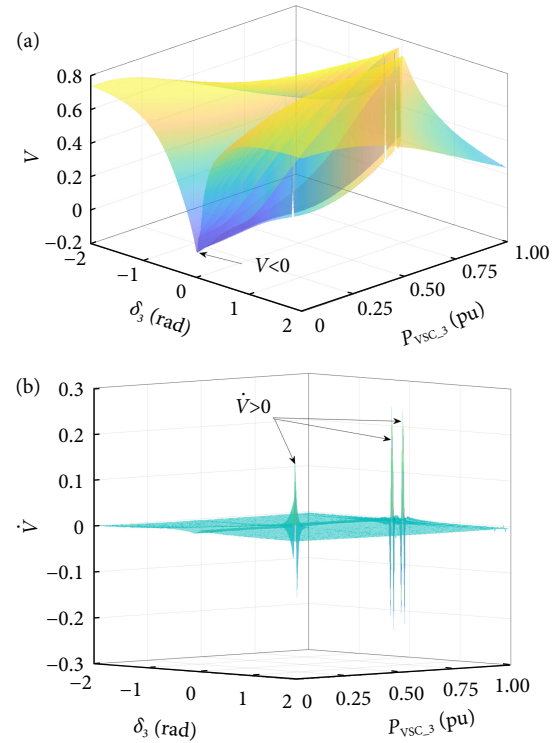

Fig. 9 (a) Lyapunov function and (b) time derivative of Lyapunov function for a grid-connected microgrid under unstable conditions.

4.2 CIGRE microgrid

The scalability of the proposed PINN technique is validated for the 12.47 kV, 60 Hz CIGRE microgrid[27], as shown in Figure 10. Single-phase networks are connected at buses 2, 5, 13, and 14. The system is managed by 8 VSCs of capacities 20 kW, 20 kW, 663 kW, 1.5 MW, 30 kW, 552 kW, 254 kW and 10 kW with droop control connected at buses 3, 4, 6, 7, 8, 9, 10, and 11, respectively. Case is simulated where switches S_1, S_2, S_3, and S_4 are opened at 1 s. VSCs and loads at buses 7, 8, 9, 10, and 11 are disconnected from the system. For the remaining system, a Lyapunov function is learned in 137.2566 s. Figures 11(a) and 11(b) show the learned Lyapunov function with positive definite, holding $V(x(0)) = 0.268 > 0$ and its time derivative with negative definite, respectively, for the contingency. This suggests that the learned Lyapunov function can be used for the TSA of the CIGRE microgrid after the source and load disconnection.

The time domain simulation results of output power P and δ at buses 3, 4, and 6 in Figures 12(a) and 12(b) show that $P_{\text{VSC\_3}}$, $P_{\text{VSC\_4}}$, $P_{\text{VSC\_3}}$, δ_3, δ_4 and δ_6 attain their equilibrium values after a disturbance at 1 s. Similarly, all state variables tend to their pre-dispatched value and the system attains its stability after generation
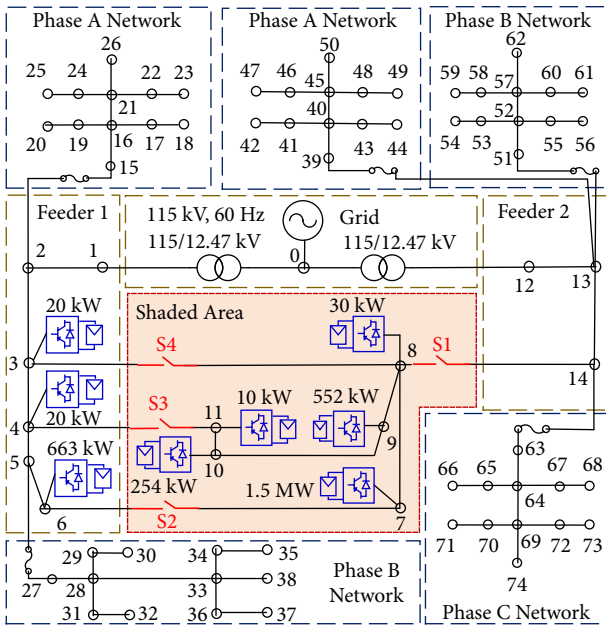
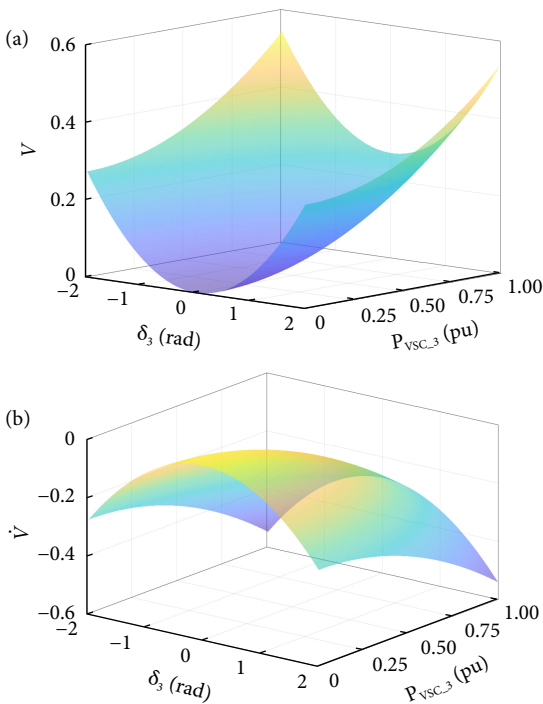**Fig. 10** CIGRE microgrid with 8 VSCs at buses 3, 4, 6, 7, 8, 9, 10, and 11.

Fig. 11 (a) Lyapunov function and (b) its time derivative for CIGRE microgrid.

disconnection and load shedding.

5 Comparative assessment

The proposed PINN Lyapunov approach is compared with the neural Lyapunov method in Ref. [21] for TSA of microgrid shown in Figure 5. The operating condition of the system is already discussed in Section 4.1 in detail. Different cases studied for this purpose are discussed in detail in the following sections.

5.1 Prediction accuracy

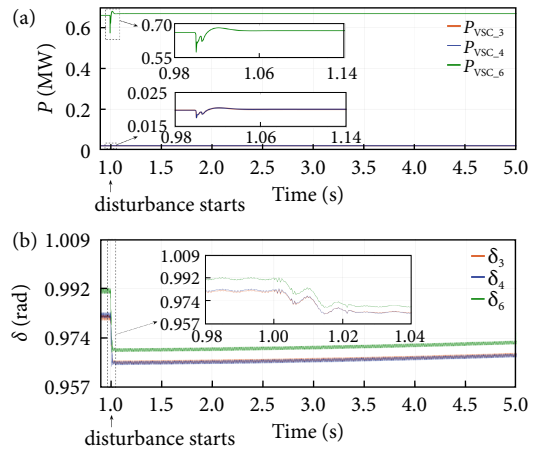The level of accuracy of the PINN approach is compared with NN

Fig. 12 (a) Power output of VSCs and, (b) bus voltage angle with time after shedding an area in CIGRE system.

for a given dataset for each case. The deep neural network structure varies in the number of layers (N_{layer}) and the number of neurons (N_{Neuron}) in each layer for each case. Figure 13 shows the prediction accuracy with PINN and NN approach for different combinations of $N_{\text{Neuron}} \times N_{\text{layer}}$. It is observed that PINNs consistently outperform simple NN across all tested combinations. With the number of layers, the prediction accuracy increases, whereas only using more neurons per layer leads to insignificant accuracy improvements. This is because PINN evaluates the dynamic of the system additionally to improve the accuracy of the output for a given limited data point. The incorporation of more ayers using physics provides a clear benefit over a simple NN.
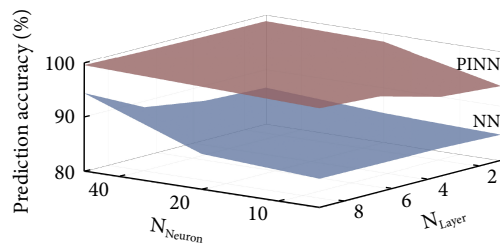

Fig. 13 Comparison of prediction accuracy of PINN and NN.

To evaluate the performance of the learned Lyapunov function for each class, a classification report is given in Table 1. The report provides a summary of metrics that describe the function's performance, such as precision, recall, and F1-score for different combinations of N_{Neuron} and N_{Layer}. The predicted dataset is of continuous type; therefore, a cut-off of 0.7 is chosen to get balanced datasets for class 0 and class 1. It is observed that the combination 20×8 results in a high precision score (closer to 1) for class 0 and class 1. Similar results are obtained for combination 40×8. High precision demonstrates the model's ability to make fewer false positive errors at the cost of the recall, i.e. 0.62 for class 1. To provide a balanced assessment of a model's performance, F1 score metric takes into account both precision and recall. For class 0, both high precision and high recall result in a high F1 score, whereas for class 1, F1 score is helping to strike a balance between high precision and low recall. On the contrary, for both training models, the weighted average accuracy remains constant as it is not much affected by the increase in neurons per layer.

5.2 Evaluation loss

An over-fitting problem frequently occurs in many machine

Table 1　Classification report

	$N_{\text{Neuron}} = 20, N_{\text{layer}} = 8$			$N_{\text{Neuron}} = 40, N_{\text{layer}} = 8$		
	Precision	Recall	F1 score	Precision	Recall	F1 score
Class 0	0.99	1.00	0.99	0.98	1.00	0.99
Class 1	0.93	0.62	0.75	0.94	0.62	0.74
Accuracy			0.98			0.98
Macro avg	0.95	0.81	0.87	0.97	0.81	0.87
Weighted avg	0.98	0.98	0.98	0.98	0.98	0.98

learning models. Figure 14 shows the evaluation loss on the validation of the data set with respect to epoch. It is observed that until 70 epochs, both PINN and NN quickly reduce the loss, however, afterward, only the PINN can improve the performance on the validation set. Hence, continuing the training process leads to reducing the evaluation loss at the expense of longer computation time with each epoch.
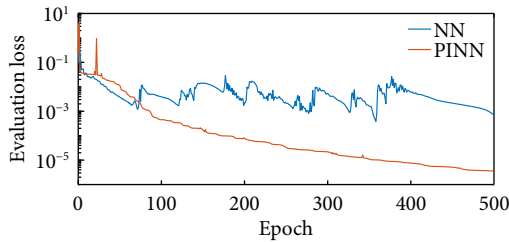

Fig. 14　Comparison of evaluation loss of PINN and NN.

5.3　Comparison with traditional methods

Table 2 provides a comprehensive comparative assessment of the proposed physics-informed method with traditional transient stability assessment methods, such as time-domain simulation, energy function methods, modal analysis, and machine learning techniques. Each method is evaluated across accuracy, complexity, applicability, and data requirements criteria. Time-domain methods are highly accurate, but, higher complexity for non-linear VSC dilutes its applicability to microgrids. Modal analysis methods are less complex, but, require a detailed system model which is not practically available due to variable control options in VSCs. Energy function-based methods are moderately accurate and complex. The inclusion of data-driven neural techniques with energy functions may further reduce the complexity of the method; however, it requires large training datasets. On the contrary, the proposed method provides highly accurate solutions for each microgrid connected to the grid. In the method, the model physics is directly incorporated into the deep neural networks, therefore, requiring less training dataset. This comprehensive comparison highlights the strengths of the proposed approach and the limitations of traditional methods in assessing the transient stability of the VSC-interfaced microgrid.

6　Conclusions

Different control algorithms embedded in VSCs influence the internal voltages and associated source impedance. Moreover, microgrids consist of short lines with high R/X ratio. Therefore, the conventional transient (angle) stability assessment technique finds limitations in the presence of the converter-controlled VSC in a microgrid. In addition, the computation of the conventional Lyapunov function is very time-consuming for such large systems with converter dynamics. To access the transient stability of the VSC-interfaced microgrid, physics informed neural Lyapunov approach is proposed in this paper. The method incorporates the dynamics of the system and initial and boundary conditions for learning the Lyapunov function in state space. The effectiveness of the approach is tested on a grid-connected microgrid for fault and droop coefficient variation cases and a CIGRE microgrid for generator outage and load-shedding cases. Simulation results validate that the proposed method does not require microgrid dynamics. A comparative assessment of the proposed PINN Lyapunov with the simple neural Lyapunov and traditional methods demonstrates the strength of the proposed approach in transient stability assessment of the VSC-interfaced microgrid, where the parameters of the VSC are influenced by the irradiance level. Future research direction will be the examination of the influence of other intermittent sources like wind power generation on the VSC parameter variation.

Appendix

The voltage relation for the circuit (see Figure 1) is as follows,

$$V_{\text{o}}\angle\delta = E_{\text{VSC}}\angle\varphi - I_{\text{o}}\angle\phi\, Z_{\text{VSC}}\angle\theta_{\text{VSC}}, \tag{30}$$

Separating real and imaginary parts and rearranging, Eq. (30) can be rewritten as

$$\begin{bmatrix} V_{\text{o}}\cos\delta \\ V_{\text{o}}\sin\delta \end{bmatrix} = \begin{bmatrix} 1\ 0\ -I_{\text{o}}\cos\phi\ \ I_{\text{o}}\sin\phi \\ 0\ 1\ -I_{\text{o}}\sin\phi\ -I_{\text{o}}\cos\phi \end{bmatrix} \begin{bmatrix} E_{\text{VSC}}\cos\varphi \\ E_{\text{VSC}}\sin\varphi \\ R_l \\ X_l \end{bmatrix}, \tag{31}$$

The simplified form of Eq. (31) can be

Table 2　Comparison of proposed and traditional transient stability assessment methods

Methods	Accuracy	Complexity	Applicability	Data requirements
Time-domain simulation[28, 29]	High	High	Small to medium	Detailed system models
Energy function method[14, 15]	Moderate	Moderate	Small to large	System parameters
Modal analysis[16–18]	Moderate	Low	Small to large	Detailed system models
Neural network technique[19–21]	Variable	Low to moderate	Small to medium	Large training dataset
Proposed method	Very high	Low	Small to large	Less training dataset

$$[V] = [I][B], \qquad (32)$$

where $[V]$ and $[I]$ are corresponding voltage and current matrices, respectively. Matrix $[B]$ contains internal voltages and impedances of VSC. The unknown parameters in $[B]$ can be computed as

$$[B] = [(I'I)^{-1}I][V]. \qquad (33)$$

On solving Eq. (33), real and imaginary components of E_{VSC} and Z_{VSC} can be obtained from Ref. [11].

Acknowledgments

Article history

Additional information

Declaration of competing interest

The authors have no competing interests to declare that are relevant to the content of this article.

References

[1] Farrokhabadi, M., Canizares, C. A., Simpson-Porco, J. W., Nasr, E., Fan, L., Mendoza-Araya, P. A., Tonkoski, R., Tamrakar, U., Hatziargyriou, N., Lagos, D., et al. (2020). Microgrid stability definitions, analysis, and examples. *IEEE Transactions on Power Systems*, 35: 13–29.

[2] Zhang, P. (2021). *Networked Microgrids*. Cambridge: Cambridge University Press.

[3] Zhang, Y., Xie, L. (2016). A transient stability assessment framework in power electronic-interfaced distribution systems. *IEEE Transactions on Power Systems*, 31: 5106–5114.

[4] Kundur, P., Malik, O. (2022). *Power System Stability and Control, 2nd edn.* McGraw-Hill Education.

[5] Sauer, P., Pai, M. (1998). *Power System Dynamics and Stability*. Prentice Hall.

[6] Zhong, Q. C., Weiss, G. (2011). Synchronverters: Inverters that mimic synchronous generators. *IEEE Transactions on Industrial Electronics*, 58: 1259–1267.

[7] Shintai, T., Miura, Y., Ise, T. (2014). Oscillation damping of a distributed generator using a virtual synchronous generator. *IEEE Transactions on Power Delivery*, 29: 668–676.

[8] Chen, Y., Hesse, R., Turschner, D., Beck, H. P. (2011). Improving the grid power quality using virtual synchronous machines. In: Processing of the 2011 International Conference on Power Engineering, Energy and Electrical Drives, Malaga, Spain.

[9] Majumder, R., Chaudhuri, B., Ghosh, A., Majumder, R., Ledwich, G., Zare, F. (2010). Improvement of stability and load sharing in an autonomous microgrid using supplementary droop control loop. *IEEE Transactions on Power Systems*, 25: 796–808.

[10] Sun, H., Lin, X., Huang, G., Zhang, J., Liu, D., Jiang, K., Kang, Y. (2023). The transient instability mechanism and stability-enhanced

[11] Mishra, P., Pradhan, A. K., Bajpai, P. (2021). Adaptive distance relaying for distribution lines connecting inverter-interfaced solar PV plant. *IEEE Transactions on Industrial Electronics*, 68: 2300–2309.

[12] Pogaku, N., Prodanovic, M., Green, T. C. (2007). Modeling, analysis and testing of autonomous operation of an inverter-based microgrid. *IEEE Transactions on Power Electronics*, 22: 613–625.

[13] Nagrath, I. J., Kothari, D. P., Desai, R. C. (1982). Modern power system analysis. *IEEE Transactions on Systems, Man, and Cybernetics*, 12: 96–96.

[14] Chiang, H. D. (1989). Study of the existence of energy functions for power systems with losses. *IEEE Transactions on Circuits and Systems*, 36: 1423–1429.

[15] Vu, T. L., Turitsyn, K. (2016). Lyapunov functions family approach to transient stability assessment. *IEEE Transactions on Power Systems*, 31: 1269–1277.

[16] Kabalan, M., Singh, P., Niebur, D. (2017). Large signal Lyapunov-based stability studies in microgrids: A review. *IEEE Transactions on Smart Grid*, 8: 2287–2295.

[17] Kabalan, M., Singh, P., Niebur, D. (2019). Nonlinear Lyapunov stability analysis of seven models of a DC/AC droop controlled inverter connected to an infinite bus. *IEEE Transactions on Smart Grid*, 10: 772–781.

[18] Huang, T., Sun, H., Kim, K. J., Nikovski, D., Xie, L. (2020). A holistic framework for parameter coordination of interconnected microgrids against disasters. In: Processing of the 2020 IEEE Power & Energy Society General Meeting (PESGM), Montreal, QC, Canada.

[19] He, M., Zhang, J., Vittal, V. (2013). Robust online dynamic security assessment using adaptive ensemble decision-tree learning. *IEEE Transactions on Power Systems*, 28: 4089–4098.

[20] Xu, Y., Dong, Z. Y., Zhao, J. H., Zhang, P., Wong, K. P. (2012). A reliable intelligent system for real-time dynamic security assessment of power systems. *IEEE Transactions on Power Systems*, 27: 1253–1263.

[21] Huang, T., Gao, S., Xie, L. (2022) A neural Lyapunov approach to transient stability assessment of power electronics-interfaced networked microgrids. *IEEE Transactions on Smart Grid*, 13: 106–118.

[22] Raissi, M., Perdikaris, P., Karniadakis, G. E. (2017). Physics informed deep learning (Part I): Data-driven solutions of nonlinear partial differential equations. *arXiv preprint*, 1711.10561.

[23] Stiasny, J., Misyris, G. S., Chatzivasileiadis, S. (2021). Transient stability analysis with physics-informed neural networks. *arXiv preprint*, 2106.13638.

[24] Mishra, P., Pradhan, A. K., Bajpai, P. (2019). Voltage control of PV inverter connected to unbalanced distribution system. *IET Renewable Power Generation*, 13: 1587–1594.

[25] Lin, H., Jia, C., Guerrero, J. M., Vasquez, J. C. (2017). Angle stability analysis for voltage-controlled converters. *IEEE Transactions on Industrial Electronics*, 64: 6265–6275.

[26] E, W., Ma, C., Wojtowytsch, S., Wu, L. (2020). Towards a mathematical understanding of neural network-based machine learning: What we know and what we don't. *arXiv preprint*, 2009.10713.

[27] Strunz, K., Abbasi, E., Fletcher, R., Hatziargyriou, N. D., Iravani, R., Joos, G. (2014). TF C6.04.02: TB 575 – Benchmark Systems for Network Integration of Renewable and Distributed Energy Resources. CIGRE.

[28] Xue, Y., Van Custem, T., Ribbens-Pavella, M. (1989). Extended equal area criterion justifications, generalizations, applications. *IEEE Transactions on Power Systems*, 4: 44–52.

[29] Xue, Y., Pavella, M. (1989). Extended equal-area criterion: An analytical ultra-fast method for transient stability assessment and preventive control of power systems. *International Journal of Electrical Power & Energy Systems*, 11: 131–149.